

Interrelations between Printing Patterns and Residual Stress in Fused Deposition Modelling for the 4D Printing of Acrylonitrile Butadiene Styrene and Wood–Plastic Composites

Yerong Huang ¹, Sandra Löschke ², Yixiang Gan ¹ and Gwénaëlle Proust ^{1,3,*}

¹ School of Civil Engineering, The University of Sydney, Sydney, NSW 2006, Australia; yerong.huang@sydney.edu.au (Y.H.); yixiang.gan@sydney.edu.au (Y.G.)

² Sydney School of Architecture, Design and Planning, The University of Sydney, Sydney, NSW 2006, Australia; sandra.loschke@sydney.edu.au

³ The Sydney Manufacturing Hub, The University of Sydney, Sydney, NSW 2006, Australia

* Correspondence: gwenaelle.proust@sydney.edu.au

Abstract: Four dimensional printing enables the advanced manufacturing of smart objects that can morph and adapt shape over time in response to stimuli such as heat. This study presents a single-material 4D printing workflow which explores the residual stress and anisotropy arising from the fused deposition modelling (FDM) printing process to create heat-triggered self-morphing objects. In particular, the study first investigates the effect of printing patterns on the residual stress of FDM-printed acrylonitrile butadiene styrene (ABS) products. Through finite element analysis, the raster angle of printing patterns was identified as the key parameter influencing the distribution of residual stresses. Experimental investigations further reveal that the non-uniform distribution of residual stress results in the anisotropic thermal deformation of printed materials. Thus, through the design of printing patterns, FDM-printed materials can be programmed with desired built-in residual stresses and anisotropic behaviours for initiating and controlling the transformation of 4D-printed objects. Using the proposed approach, any desktop FDM printers can be turned into 4D printers to create smart objects that can self-morph into target geometries. A series of 4D printing prototypes manufactured from conventional ABS 3D printing feedstock are tested to illustrate the use and reliability of this new workflow. Additionally, the custom-made wood–plastic composite (WPC) feedstocks are explored in this study to demonstrate the transposability of the 4D printing approach.

Keywords: additive manufacturing; 4D printing; FDM; residual stress; anisotropy; finite element analysis

Citation: Huang, Y.; Löschke, S.; Gan, Y.; Proust, G. Interrelations between Printing Patterns and Residual Stress in Fused Deposition Modelling for the 4D Printing of Acrylonitrile Butadiene Styrene and Wood–Plastic Composites. *J. Manuf. Mater. Process.* **2024**, *8*, 77. <https://doi.org/10.3390/jmmp8020077>

Academic Editor: Steven Y. Liang

Received: 29 February 2024

Revised: 2 April 2024

Accepted: 11 April 2024

Published: 15 April 2024



Copyright: © 2024 by the author. Licensee MDPI, Basel, Switzerland. This article is an open access article distributed under the terms and conditions of the Creative Commons Attribution (CC BY) license (<https://creativecommons.org/licenses/by/4.0/>).

1. Introduction

Additive manufacturing, commonly known as 3D printing, has triggered industrial innovations by offering unprecedented design opportunities to turn complex digital models into physical products by adding materials layer upon layer. Four-dimensional printing further presents a new paradigm in additive manufacturing. It is a concept first introduced to address the extensive post-processing required by complex 3D-printed geometries [1]. The fourth dimension refers to the capability of a 3D-printed object to transform over time when subjected to external stimuli. Through the design of material systems and control of the manufacturing process, 4D-printed products are programmed with the self-morphing functionality that can be activated by various environmental changes such as heat [2–9], moisture [10–15], pH [16–20], electricity [21–24], and magnetic field [25–30]. It offers the possibilities to fabricate objects that can self-transform from

simple into complex geometries, reducing the need for support structures, minimizing the production time, and saving manufacturing costs. This opens up the potential of conventional additive manufacturing technologies in new areas of applications, such as deployable architectures [31–34], smart textile [35–37], self-folding packaging [38–44], wearable devices [45–47], and soft robotics [48–51].

While various additive manufacturing technologies have been reported to successfully achieve 4D printing [25,48,50,52–54], fused deposition modelling (FDM) has become a particular research interest due to the low printing costs, easy access to desktop FDM printers, and broad range of printing materials [55,56]. FDM is a material extrusion-based additive manufacturing process, whereby the filament materials are first melted through a heated nozzle and then deposited on a build platform following specific printing paths to produce 3D objects [55]. Most FDM-based 4D printing studies focus on shape-memory polymers (SMPs), which are smart materials capable of retaining a temporary shape and recovering their original shape when heated above the glass transition temperature (T_g) [57–62]. However, the temporary shape of the printed SMP products has to be manually programmed, which significantly limits the potential of FDM-based 4D printing. Although a new approach that employs multi-material systems to create bilayer actuating structures composed of an active layer and a passive layer has been reported [24,40,63–68], these multi-material systems require either FDM printers equipped with dual nozzles to print the different materials or additional printing steps to switch the filaments, which complicates the manufacturing process.

As such, there has been a growing interest in developing single-material 4D printing methods which utilise the residual stress in FDM-printed materials as the activation energy to initiate the self-morphing mechanism [69–76]. Residual stresses are self-equilibrating stresses that remain in materials in the absence of any external loads. During FDM printing, the deposited materials are subjected to rapid heating and cooling cycles while being constrained to the printer bed or previously printed layers, resulting in the build-up of residual stresses [77,78]. The presence of residual stress can lead to a distinct thermal shrinking behaviour of FDM-printed materials [69,79]. A study that explored the pattern transformations of 2D lattice structures under heating first reports that FDM-printed polylactic acids (PLAs) shrink when heated above the glass transition temperature [69]. It suggests that this phenomenon is attributed to the release of residual stress under the thermal stimulus.

Combining this distinct thermal shrinking behaviour with the anisotropy exhibited by FDM-printed products, researchers have been able to create various heat-triggered morphing structures, including deploy mesh surfaces [70], rising tiles [71], and linear structures capable of bending in eight directions [72]. Material and structural anisotropies have been shown previously to be a good way to control morphing properties [80–83], and FDM offers a new way to control the anisotropy of a printed component by varying the printing parameters [84]. Experimental and numerical studies have been carried out to investigate the effect of various FDM printing parameters, including the printing layer thickness, printing speed, and nozzle diameter, on the shrinkage rate, and torsional and flexural deformation behaviour of 4D-printed PLA structures [61,73,74]. Lately, researchers have also focused on computational simulations to model the morphing process of FDM-based 4D-printed objects. A constitutive model was developed to describe the thermos–mechanical behaviour of PLA during the FDM printing process to predict the temperature-driven deformation of 4D-printed PLA monolayers [75]. A finite element model that characterises the effective thermal expansion coefficient of acrylonitrile butadiene styrene (ABS) printed with different directions was established to predict the thermal deformation of 4D-printed ABS products [76].

However, despite these case studies successfully demonstrating the feasibility of FDM-based single-material 4D printing, few studies have looked into the residual stress developed within the FDM-printed components. The only research that has explored residual stresses investigates the stress gradient between the top and bottom layers

without considering the printing pattern effect [73]. In most of the reported numerical simulations, the residual stress of FDM-printed components was estimated based on trial and error until the predicted morphing shapes match the experimental observations. In addition, despite the diverse printing materials available, the current research on single-material 4D printing has mainly focused on commercial thermoplastic filaments, such as PLA and ABS, without exploring the potential of custom-made composite filaments.

This research aims to provide deeper insights into the residual stress arising from the FDM printing process, and to design a temperature-based 4D printing workflow that enables the printed objects to self-morph into desired forms when triggered by heat. More specifically, a finite element method (FEM) modelling framework was developed in this project to simulate the residual stress of FDM-printed components and predict the morphing process of the 4D-printed products. The effect of printing patterns on the residual stress of FDM-printed products was first explored through FEM analysis. Based on the numerical findings, a temperature-based 4D printing approach was then proposed, which utilises the residual stress and anisotropy as the morphing principles to initiate and control the shape transformation. A variety of physical prototypes, printed from commercial ABS filaments and custom-made wood–plastic composite (WPC) filaments, are presented in this project. The outcomes of this research offer opportunities to deliver an accessible and sustainable solution to achieving complex forms using a simple production process.

2. Materials and Methods

2.1. Finite Element Method (FEM) Modelling

The FDM printing process and the heat-triggered morphing process of 4D-printed objects were modelled using the FEM in Abaqus 2020 (Simulia, Dassault Systèmes). The modelling framework is shown in Figure 1. Two sets of sequential thermal–mechanical FEM models were developed to simulate the residual stress of FDM-printed objects and predict the final transformed shapes of the 4D-printed objects. In both FEM models, meshing elements with dimensions of 0.4 mm × 0.4 mm × 0.2 mm and a time step of 0.5 s were used based on sensitivity analysis. For the thermal analysis, 8-node linear diffusive heat transfer DC3D8 elements were used. For the mechanical analysis, full-integration solid C3D8 elements were used.

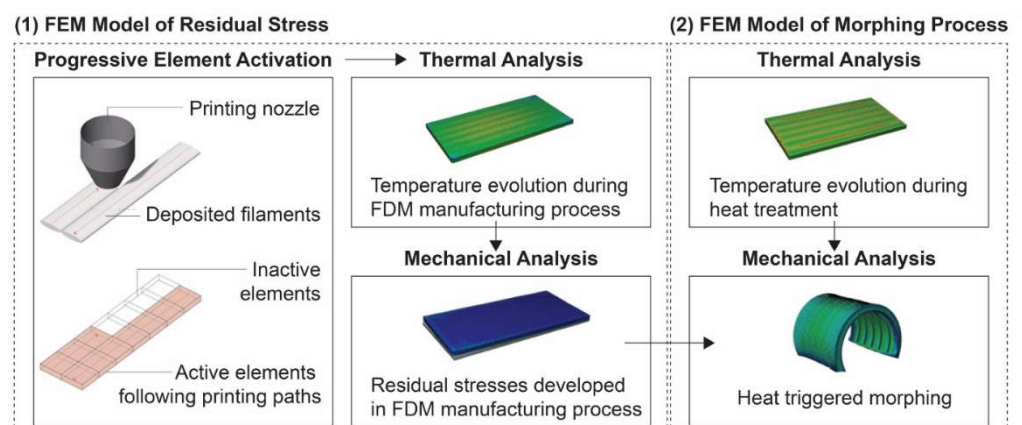


Figure 1. Framework of sequential thermal–mechanical FEM models to simulate the creation of residual stress during FDM and predict the heat-triggered morphing process of 4D-printed objects.

In the first FEM model, both the FDM-printed object and the printer bed were included. The printed object and the printer bed were assumed to be homogeneous with isotropic material properties. To simulate the material deposition process of FDM printing, the progressive element activation technique with an in-house Grasshopper

script was used. The elements of the printed object were activated sequentially according to the user-defined printing paths. For simplicity, the cross-section of the deposited filaments was assumed to be rectangular and the voids present in 3D-printed objects were neglected.

A transient heat transfer analysis, consisting of a printing step and a cooling step, was first performed to obtain the temperature evolution during the FDM manufacturing process. Initial conditions of temperature T_p corresponding to the printing temperature and temperature T_b corresponding to the bed temperature were assigned to the 3D-printed object and the printer bed, respectively. The constant temperature T_b was also assigned to the printer bed as a boundary condition in the printing step. A tie constraint was applied to connect the 3D-printed object and the printer bed to model the heat conduction. The convection and radiation cooling of the deposited materials during printing was modelled by defining the film coefficient and emissivity on the free surfaces of the printed parts. In the cooling step, the convection and radiation cooling were applied to both the 3D-printed object and the printer bed. The history of the nodal temperature of the 3D-printed objects and the printer bed was recorded.

Static structural analysis was performed subsequently to evaluate the residual stress. Initial temperatures of T_p and T_b were assigned to the printed object and the printer bed, respectively. The bottom of the printer bed was fixed in all degrees of freedom as a boundary condition. A tie constraint was also applied to connect the printed object with the printer bed. The temperature evolution determined from the previous thermal analysis was introduced in the printing and cooling steps as thermal loads to calculate the resultant stress distribution. An additional bed removal step was included to model the detaching procedure, in which the elements of the printer bed were removed to allow for the printed object to deform freely. The nodal displacement, stress, and strain experienced by the printed object were calculated.

In the second FEM model, only the FDM-printed object was included. Although the object was printed from a single material, the deposited materials exhibit anisotropic thermal behaviours because of the residual stress effect. Thus, two sets of anisotropic thermal expansion coefficients were defined for materials printed along the transverse and longitudinal directions. A transient heat transfer analysis was first performed to obtain the temperature evolution of the printed object during the heat treatment. The initial temperature of the printed object was set at room temperature, which was assumed to be 25 °C. The heat treatment was modelled as convection and radiation heating. The film coefficient and emissivity were assigned to the free surfaces of the printed object with an ambient temperature of 125 °C corresponding to the oven temperature. In the subsequent static structural analysis, the obtained temperature evolution of the printed object during the heat treatment was included as the thermal load. The residual stresses determined from the first FEM model was assigned to the printed object as the initial stress state. The resultant nodal displacement, stress, and strain experienced by the printed object were determined.

2.2. Materials and FDM Printing Parameters

Two types of thermoplastic materials, ABS and WPC, were employed in this research. ABS is an amorphous thermoplastic polymer that has been widely used in FDM for prototyping. It is a low-cost printing material that shows high impact and abrasion resistance, toughness, and strong resistance to weathering [85–88]. WPC is a commonly used green alternative to natural timber products which offers a low environmental footprint with the opportunity for sustainable manufacturing through the recycling of forestry by-products and thermoplastics [89,90]. In this paper, this second material was used to prove that the morphing phenomena are repeatable in different materials and that material properties affect the level of morphing capability.

The FEM analysis was performed for ABS to demonstrate that the framework can be used for prediction and design in future applications. An elasto-plastic constitutive model

was used to model the thermo-plastic behaviour of ABS [91]. The common properties of ABS are summarised in Table 1 [91–93]. The temperature-dependent thermal and mechanical properties of ABS used in the FEM analysis are summarised in Figure 2 [94–97]. The material of the printer bed included in the first FEM model was Borosilicate glass. The properties of Borosilicate glass, from the standard ISO 3585:1998 Borosilicate glass 3.3—Properties, are summarised in Table 2 [98].

Table 1. Common material properties of ABS used in FEM analysis.

Density ($\times 10^{-12}$ t/mm ³)	Thermal Expansion Coefficient ($\times 10^{-6}$ °C ⁻¹)	Poisson’s Ratio	Emissivity	Film Coefficient (mW/mm ² °C)
1050	90	0.32	0.92	8×10^{-3}

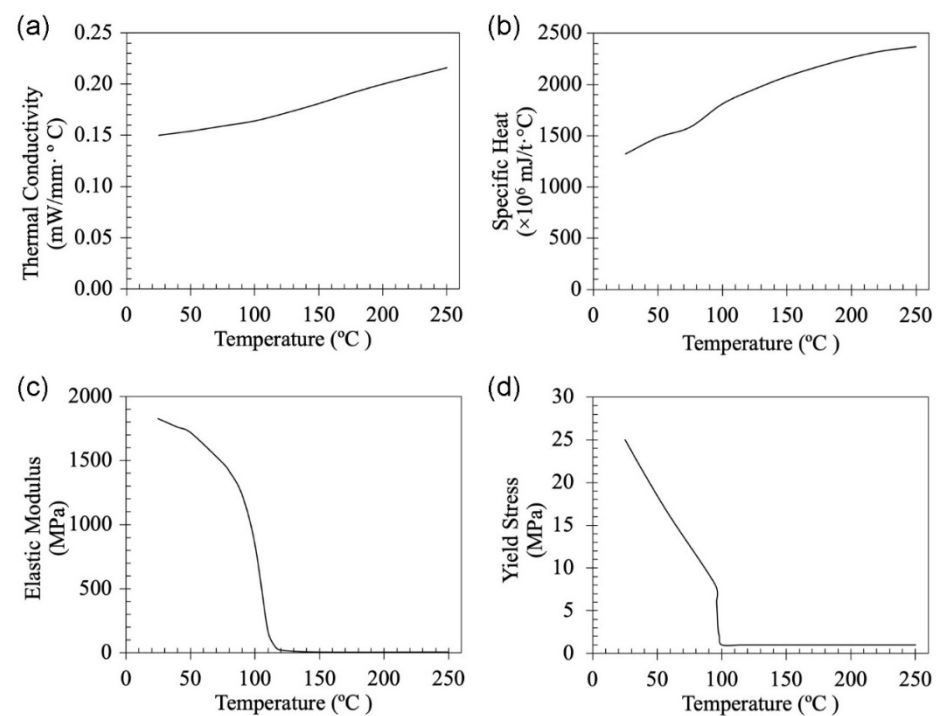


Figure 2. Temperature-dependent thermal and mechanical properties of ABS used in FEM analysis: (a) thermal conductivity; (b) specific heat; (c) elastic modulus; (d) yield strength.

Table 2. Material properties of Borosilicate glass used in FEM analysis.

Density ($\times 10^{-12}$ t/mm ³)	Thermal Conductivity (mW/mm·°C)	Specific Heat ($\times 10^6$ mJ/t·°C)	Thermal Expansion Coefficient ($\times 10^{-6}$ °C ⁻¹)	Elastic Modulus (MPa)	Poisson’s Ratio
2230	1.2	900	3.30	64,000	0.20

The physical prototypes of the proposed temperature-based 4D printing system were manufactured using commercial ABS filaments and custom-made WPC filaments. The FDM printing parameters for the ABS and WPC filaments are summarised in Table 3. The off-the-shelf ABS filament with a diameter of 2.85 mm (Martogg Group of Companies) was first used to print the prototypes. The proposed temperature-based 4D printing approach was then applied to WPCs to create timber-like morphing objects and demonstrate the transposability of the approach. The custom-made WPC filament with a diameter of 2.75 ± 0.10 mm, consisting of 19 wt% Red Gum wood particles with sizes less than 90 μ m, 80 wt% ABS, and 1 wt% maleic anhydride that served as a binding agent, was

produced at an extrusion temperature of 157 °C using a Noztek Pro filament extruder. The detailed information about the filament manufacturing method can be found in the previous study by the authors [99].

Table 3. FDM printing parameters for ABS and WPC filaments.

Filament	Printing Temperature, T_p (°C)	Printer Bed Temperature, T_b (°C)	Printing Speed (mm/min)	Layer Thickness (mm)	Fill Density
ABS	245	100	1200	0.2	100%
WPC	235	110	1200	0.2	100%

2.3. Simulated Geometries and Printing Patterns

To investigate the effect of printing patterns on residual stresses, the FEM analysis was first carried out on a rectangular bar with the dimensions of 80 mm × 8.0 mm × 1.6 mm, as shown in Figure 3. A printer bed of 1.0 mm thickness was also included in the simulations. Four infill patterns shown in Figure 3 were simulated to print the bar. The printing patterns were named according to their raster angles, which were measured between the longitudinal direction of the bar and the printing paths. For all FEM simulations, the diameter of the printing nozzle was set as 0.8 mm.

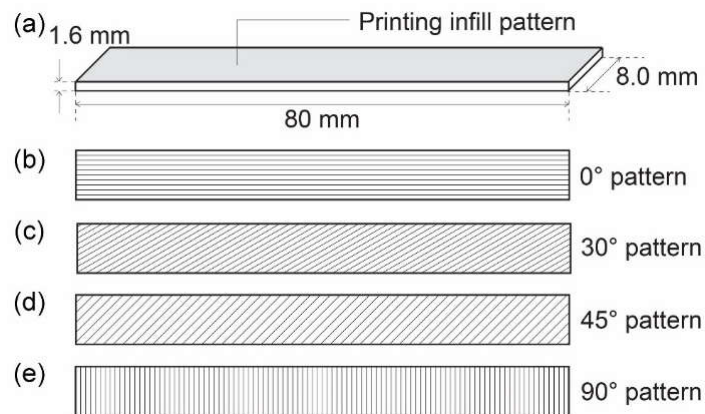


Figure 3. Simulated geometry and printing patterns of the rectangular bars for the FEM analysis: (a) the dimensions of the rectangular bar; (b–e) the infill printing patterns.

The printing patterns to achieve various shape transformations of the 4D-printed objects were designed as shown in Figure 4. Figure 4a shows the four basic printing patterns with different raster angles. Pattern A and Pattern B are printed along the transverse and longitudinal directions of the objects, respectively. Patterns C and D are printed with -45° and $+45^\circ$ raster angles, respectively. Figure 4b–d shows the different combinations of printing patterns for FDM 4D-printed objects to achieve various geometries, including concave, wavy, and spiral designs.

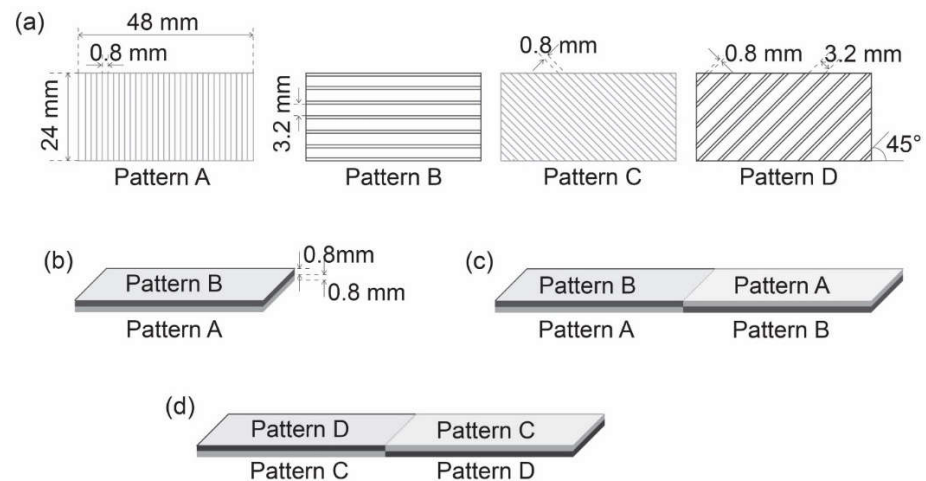


Figure 4. Design of the printing patterns of 4D-printed objects: (a) the four basic printing patterns with different raster angles; (b) the combination of the printing patterns to achieve the concave design after heat treatment; (c) the combination of the printing patterns to achieve the wave design after heat treatment; (d) the combination of the printing patterns to achieve the spiral design after heat treatment.

2.4. Experimental Methods

2.4.1. Characterisation of Thermal Shrinkage Behaviour

To characterise the thermal shrinkage behaviour of FDM-printed materials resulting from the residual stress relaxation, the effective thermal expansion coefficient, α_i , was calculated using the following equation [76]:

$$\alpha_i = \frac{1}{\Delta T} \frac{(L_i - L'_i)}{L_i}, \quad (1)$$

where the subscript i represents the Cartesian direction (x , y , or z), ΔT is the temperature change during the heat treatment, and L_i and L'_i are the directional dimensions before and after the heat treatment, respectively.

The ABS specimens printed with the 0° and 90° patterns, as shown in Figure 3b,e, were produced using a desktop FDM 3D printer (*LulzBot*) equipped with a 0.8 mm diameter printing nozzle. The FDM printing parameters for ABS can be found in Table 3. For each printing pattern, four specimens were printed. The printed ABS specimens were then placed in an electrical furnace pre-heated at $125 \pm 5^\circ\text{C}$ to perform the heat treatment. After heating for 120 s, the ABS specimens were removed from the furnace and cooled to room temperature. The dimensions of the ABS specimens before and after the heat treatment were measured using a digital calliper (*MeasumaX*). Based on the measured dimensions, the average values of the effective thermal expansion coefficients of the ABS specimens were determined and used for the FEM analysis.

2.4.2. Manufacturing of 4D-Printed Objects and Heat Treatment

The physical prototypes of the designed 4D-printed objects were manufactured using a desktop FDM 3D printer (*LulzBot*) equipped with a 0.8 mm diameter printing nozzle. The printing parameters used for the ABS and WPC filaments can be found in Table 3. To trigger the morphing process, the printed prototypes were placed in an electric furnace preheated to $125 \pm 5^\circ\text{C}$ to perform the heat treatment. The chamber temperature was monitored by a digital thermometer (*RS-41, RS PRO*) attached to the inside of the furnace. The printed prototypes were heated for 120 s while the chamber temperature was maintained at $125 \pm 5^\circ\text{C}$. The morphing process during the heat treatment was observed and recorded using a camera. After 120 s, the transformed 4D-printed objects were removed from the furnace and cooled to room temperatures.

3. Results and Discussion

3.1. Effect of Printing Patterns on Residual Stress

To study the effect of printing patterns on residual stress, the results of the FEM analysis simulating the rectangular bars printed with different infill patterns were compared. The final residual stress developed at the bottom (1st), middle (4th), and top (8th) layers of the rectangular bars after being removed from the printer bed are shown in Figure 5 in terms of von Mises stress.

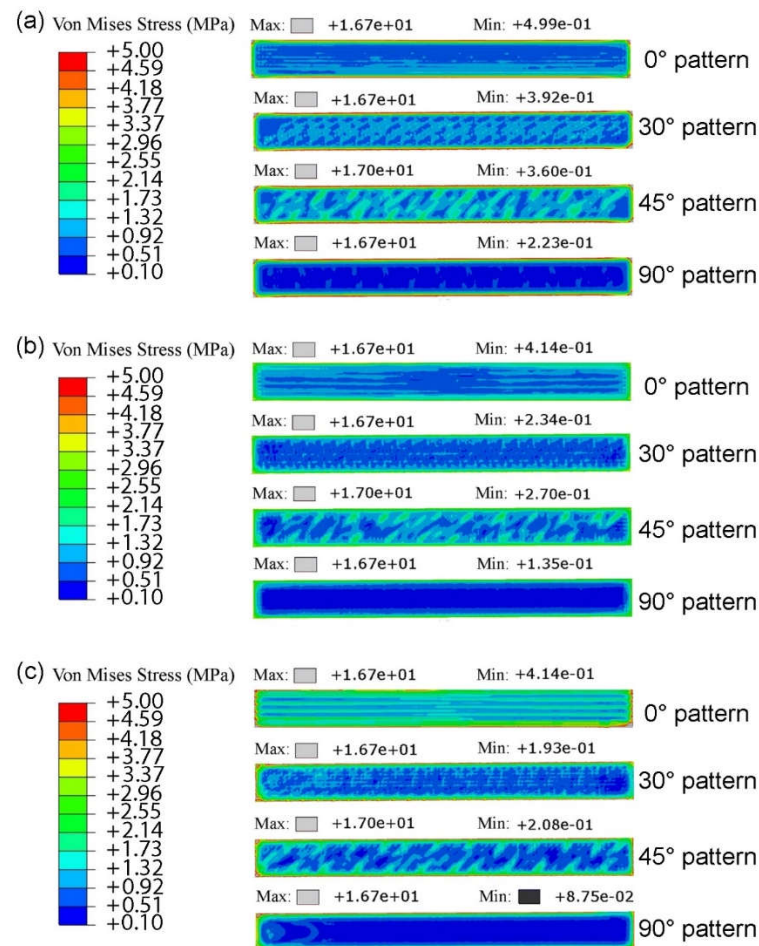


Figure 5. Residual stress of the rectangular bars printed with the different infill patterns: (a) the bottom (1st) layer; (b) the middle (4th) layer; (c) the top (8th) layer.

Non-uniform distribution of residual stress is observed for all layers with higher residual stresses located along the edges of the bars. The residual stress of the bar printed with the 90° infill pattern is distributed relatively uniformly compared to the stress for the bars printed with the other infill patterns. This can be explained by the temperature difference between the adjacent deposited filaments. Since the filament length of the 90° infill pattern is shorter than the other patterns, the deposited filament has less time to cool down before the next filament is printed. As such, the temperature difference between the adjacent filaments of the 90° infill pattern is the smallest of all patterns, resulting in the most uniform distribution of residual stress. For the other printing patterns, the distribution of residual stress is found to match the raster angle of the infill patterns.

To better understand the tensile and compressive stresses experienced by the 3D-printed objects, the residual stress components acting along the longitudinal direction of the bar (x-direction) are examined. Figure 6 shows the residual stress components of the

bars printed with the 0° and 90° infill patterns. The positive value represents the tensile stress, whilst the negative value represents the compressive stress.

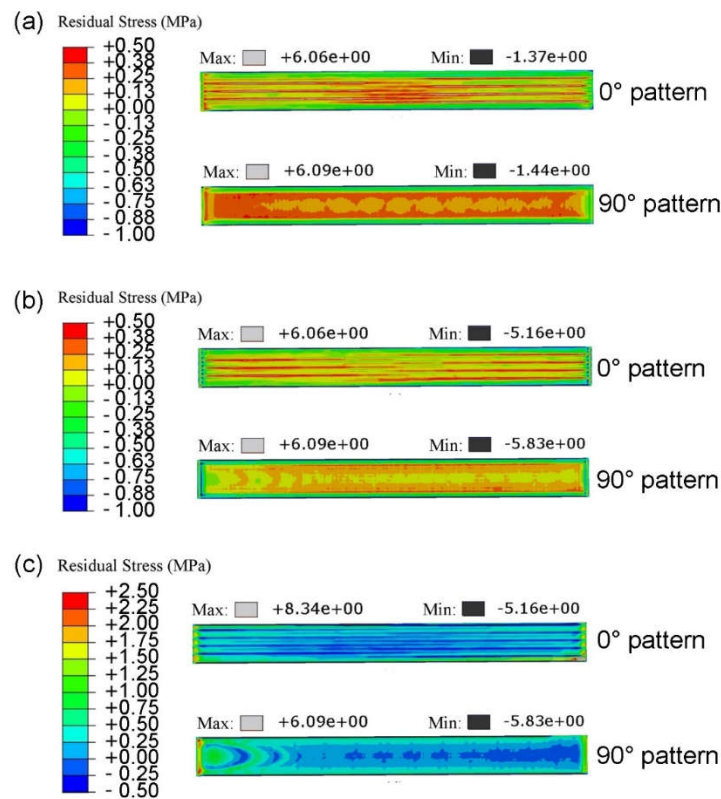


Figure 6. Residual stress acting along the x-direction of the bar printed with the 0° and 90° infill patterns: (a) the bottom layer; (b) the middle layer; (c) the top layer.

It can be seen that most of the bottom layers are in tension, except the edges where compressive stress is experienced. Such a residual stress distribution is also observed at the middle layers, yet the stress magnitude at the middle layers is much smaller than the stress at the bottom layers. This can be explained by the printing sequence of layers. Since the bottom layers were printed first, they underwent more heating and cooling cycles than higher layers, resulting in greater residual stress. The distribution of residual stress at the top layer, on the other hand, exhibits the opposite pattern. Tensile stress is observed along the edges of the bar. An alternation in tensile and compressive stress is observed at the centre of the bars. This opposite pattern of the stress distribution could be due to the fact that the top layer has a different cooling rate compared to the other layers. Since the top layer was printed last, it had a more exposed surface area than the other layers, which resulted in a higher cooling rate. Moreover, as no additional layers were printed on top, the only heating and cooling cycle experienced by the top layer was during printing. After printing, this layer only experienced cooling, whereas the lower layers underwent several heating and cooling cycles during the subsequent printing process.

The distortion of the 3D-printed rectangular bars after being removed from the printer bed is compared in Figure 7. The deflection of the bars printed with the different patterns was determined by calculating the differences in the vertical displacement of the nodes. A reduction in deflection with an increased raster angle of the infill printing pattern is observed. The bar printed with the 90° infill pattern exhibits the least deflection, which is 30.8% less than the deflection of the bar printed with the 0° infill pattern, 14.3% less than that of the bar printed with the 30° infill pattern, and 10.0% less than that of the bar printed with the 45° and the default infill patterns. The upward deflection is caused by the compressive residual stress at the top of the bar and the tensile residual stress at the

bottom of the bar in the x-direction. Since the bar printed with the 90° infill pattern has the smallest difference of residual stress between the bottom and top layers, it also displays the minimum deflection after being removed from the bed.

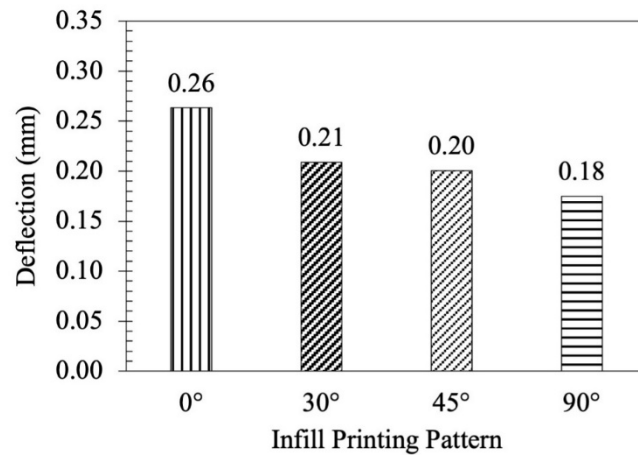


Figure 7. Deflection of the rectangular bars printed with different infill patterns.

3.2. Characterisation of Thermal Shrinkage Behaviour

The thermal shrinkage behaviour of FDM-printed materials is characterised in terms of the effective thermal expansion coefficient. The average values of the effective thermal expansion coefficient of the ABS specimens printed with the 0° pattern and 90° pattern are summarised in Table 4. The shape changes of the ABS specimens before and after the heat treatment are shown in Figure 8.

Table 4. Summary of the effective thermal expansion coefficients of the ABS specimens printed with the 0° and 90° patterns.

Effective Thermal Expansion Coefficient ($\times 10^{-3}/^{\circ}\text{C}$)	0° Printing Pattern Specimens	90° Printing Pattern Specimens
α_x	-1.80 ± 0.51	-0.21 ± 0.05
α_y	0.47 ± 0.28	-0.98 ± 0.09
α_z	2.52 ± 0.78	2.72 ± 1.12



Figure 8. Comparison of the ABS specimens before and after the heat treatment: (a) 0° printing pattern; (b) 90° printing pattern.

Both printing patterns result in anisotropic thermal deformations of the ABS specimens. Shrinkage along the printing direction and expansion along the vertical direction of the specimens are noticed. This observation agrees with the FEM analysis results discussed in Section 3.1. Since the FDM-printed materials experience tensile strains along the printing directions, the residual stress relaxation releases the pre-strain, which causes the shrinking of the materials along the printing directions.

3.3. Four-Dimensional Printing of ABS and WPC

The heat-triggered morphing process and the final transformed shapes of the 4D-printed ABS objects are shown in Figure 9, along with the FEM simulated results. For the concave design, the morphing process is also included. For all design cases, the FDM-printed ABS objects successfully transformed from flat plates into desired geometries as predicted by the FEM simulations when triggered by heat.

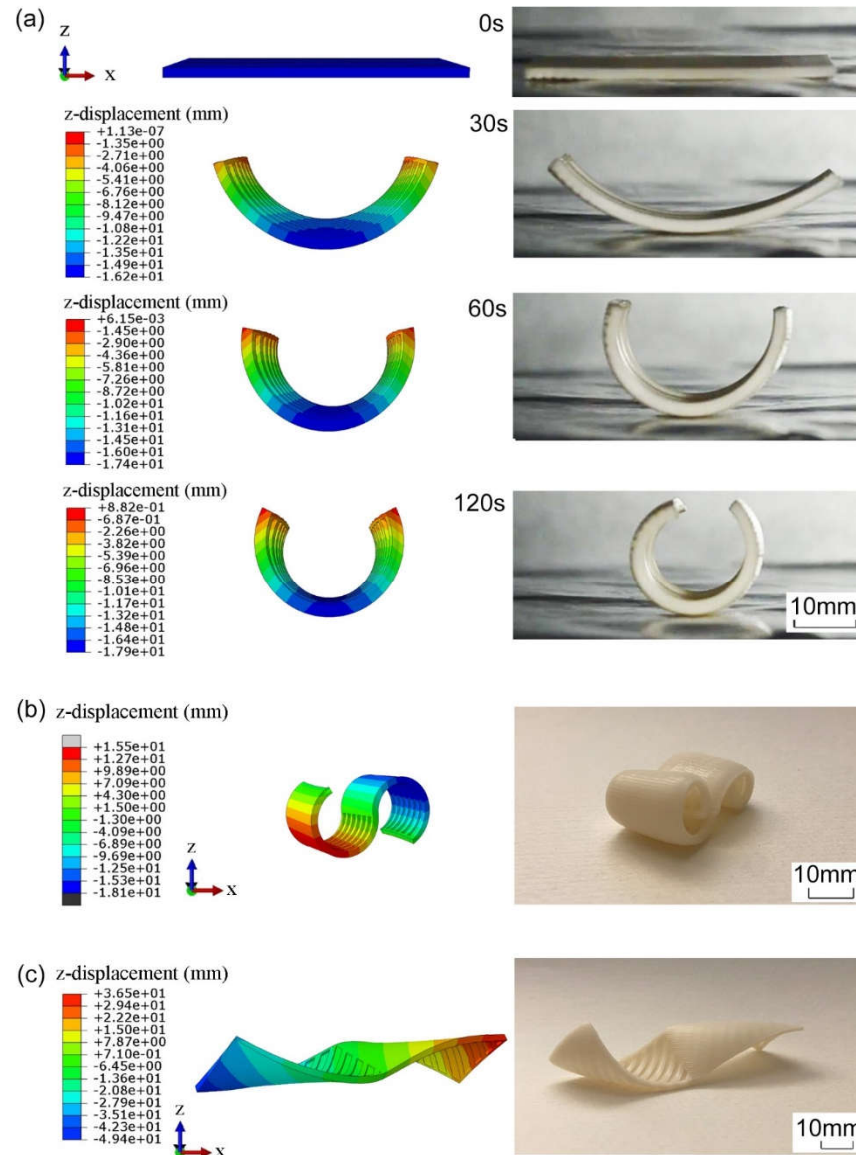


Figure 9. Four-dimensional-printed ABS objects with the FEM simulations: (a) the concave design; (b) the wave design; (c) the spiral design. The colour scale bars are different for each figure as their function is to indicate the level of deformation at each stage.

When comparing the heat-triggered morphing process shown in Figure 9a, it can be seen that the actual 4D-printed object exhibits a slight delay in the initiation of the transformation in comparison with the FEM results. This discrepancy can be explained by the temperature difference at the beginning of the heat treatment. In the FEM simulations, the furnace temperature was assumed to be perfectly constant at 125 °C. In reality, however, the furnace door was opened to place the ABS objects, causing the cooling of the temperature inside the furnace. Since the furnace temperature was lower than 125 °C at the beginning of the heat treatment, a longer time was required for the ABS objects to

reach the same temperature as the simulated results, which consequently delayed the initiation of the morphing process.

Comparing the final transformed geometries, it is notable that the 4D-printed ABS objects exhibit a slightly larger curvature than the simulated results. One possible reason for this is that the FEM analysis used a simplified elasto-plastic constitutive model to simulate the material behaviours of ABS. The thermal softening effect of ABS at higher temperatures was modelled by defining the elastic modulus as a function of temperature without considering the actual viscoelastic behaviour of ABS. Moreover, most properties of ABS defined in the current FEM analysis were averaged values taken from the literature for a similar type of ABS, which may not accurately represent the material behaviours of the ABS used in this study. However, it can be seen that the average values used in this study were able to predict the overall thermal morphing effect very well. Hence, by performing advanced thermos-viscoelastic material characterisation on the ABS used in this study, it should be possible to improve the accuracy of the current FEM. In addition, the temperature fluctuation inside the furnace during the heat treatment process could also contribute to the variations between the simulated and experimental results, as the FEM analysis assumed a constant heating temperature.

The final part of this study was to prove that the morphing effect can also be observed in more complex materials such as WPCs. The choice of this material reposes on current studies to use 3D printing to create different structural and architectural components [100]. The final transformed shapes of the 4D-printed WPC objects are shown in Figure 10, which successfully demonstrates the applicability of the proposed temperature-based 4D printing approach.



Figure 10. Final transformed shapes of 4D-printed WPC objects: (a) the concave design; (b) the wave design; (c) the spiral design.

It was noticed that 4D-printed WPC objects exhibit much less curvature than 4D-printed ABS objects for all design cases. One possible cause of this is the different residual stresses developed in the FDM-printed objects. It has been reported that the expansion coefficient of thermoplastics is reduced with the addition of wood particles [101]. Since WPC has a smaller thermal expansion coefficient than ABS, it experiences less thermal strain during the FDM manufacturing process under the same printing conditions. As the WPC objects were printed at a lower temperature compared to the ABS objects, less residual stress was developed in the WPC objects than in the ABS objects. As the residual stress is embedded in 4D-printed objects as activation energy, this leads to the smaller deformation of the WPC objects. Moreover, it has been shown that the stiffness of FDM-printed thermoplastics is improved by adding wood particles [99]. As such, the WPC objects would require greater residual stress to achieve the same amount of deformation as the ABS objects. Hence, future work on the characterisation of the material properties and numerical modelling of the residual stress in FDM-printed WPCs is recommended to better understand the morphing behaviour of 4D-printed WPC objects.

4. Conclusions

In this study, the FDM printing process was modelled using FEM to predict the residual stress developed in 3D-printed ABS products. The FEM analysis reveals that the distribution of residual stress is strongly related to the printing pattern. The 90° infill

pattern that prints along the transverse direction of the rectangular bar results in the most uniform distribution of residual stress and the least distortion of the bar. On the other hand, the 0° infill pattern, which prints along the longitudinal direction of the bar, leads to the most non-uniform distribution of residual stress and the largest distortion. As such, it is recommended to print rectangular geometries with the 90° infill pattern in order to eliminate the undesirable deformation for achieving optimum printing quality.

Based on the FEM results, a single-material temperature-based 4D printing system was then developed to manufacture heat-triggered self-morphing objects. The system utilises the residual stress developed in the FDM printing process as the activation energy to initiate the morphing process and the anisotropy introduced by the printing patterns to control the shape transformation of the printed objects. Using the proposed temperature-based 4D printing approach, thermoplastic printing materials, including ABS and WPC, can be tuned into transformable smart materials with the capability to morph from flat plates into various forms when triggered by heat. An FEM model was developed to predict the morphing process of 4D-printed ABS products. By implementing the temperature-based 4D printing workflow, any conventional desktop FDM 3D printer can be used to create objects that can self-assemble into desired forms. The findings of this project offer promising opportunities for sustainable manufacturing solutions with a simplified and faster fabrication process.

Author Contributions: Conceptualization, Y.H., S.L. and G.P.; Methodology, Y.H., Y.G. and G.P.; Validation, Y.H., Y.G. and G.P.; Formal analysis, Y.H., S.L., Y.G. and G.P.; Investigation, Y.H.; Resources, Y.G., S.L. and G.P.; Writing—original draft, Y. H.; Writing—review & editing, S.L., Y.G. and G.P.; Supervision, S.L. and G.P.; Project administration, S.L. and G.P.; Funding acquisition, S.L. and G.P. All authors have read and agreed to the published version of the manuscript.

Funding: This work was supported by Forest and Wood Products Australia in the context of the University of Sydney research project “Microtimber-Development of a 3D-printed, gradient timber panel composed of forestry waste and by-products”. FWPA is funded by industry levies and the Commonwealth Government.

Data Availability Statement: The raw data supporting the conclusions of this article will be made available by the authors on request.

Acknowledgments: The authors acknowledge the facilities and assistances of the Sydney Manufacturing Hub at the University of Sydney, and the Martogg Group Companies for their supply of polymers to support this study.

Conflicts of Interest: The authors declare no conflict of interest.

References

1. Tibbits, S. 4D printing: Multi-material shape change. *Archit. Des.* **2014**, *84*, 116–121.
2. Nishiguchi, A.; Zhang, H.; Schweizerhof, S.R.; Schulte, M.F.; Mourran, A.; Möller, M. 4D printing of a light-driven soft actuator with programmed printing density. *ACS Appl. Mater. Interfaces* **2020**, *12*, 12176–12185.
3. Kuang, X.; Roach, D.J.; Wu, J.; Hamel, C.M.; Ding, Z.; Wang, T.; Dunn, M.L.; Qi, H.J. Advances in 4D printing: Materials and applications. *Adv. Funct. Mater.* **2019**, *29*, 1805290.
4. Invernizzi, M.; Turri, S.; Levi, M.; Suriano, R. 4D printed thermally activated self-healing and shape memory polycaprolactone-based polymers. *Eur. Polym. J.* **2018**, *101*, 169–176.
5. Mahmood, A.; Akram, T.; Shenggui, C.; Chen, H. Revolutionizing manufacturing: A review of 4D printing materials, stimuli, and cutting-edge applications. *Compos. Part B Eng.* **2023**, 110952.
6. Abdullah, T.; Okay, O. 4D Printing of Body Temperature-Responsive Hydrogels Based on Poly (acrylic acid) with Shape-Memory and Self-Healing Abilities. *ACS Appl. Bio Mater.* **2023**, *6*, 703–711.
7. Lu, X.; Ambulo, C.P.; Wang, S.; Rivera-Tarazona, L.K.; Kim, H.; Searles, K.; Ware, T.H. 4D-printing of photoswitchable actuators. *Angew. Chem. Int. Ed.* **2021**, *60*, 5536–5543.
8. Rastogi, P.; Kandasubramanian, B. Breakthrough in the printing tactics for stimuli-responsive materials: 4D printing. *Chem. Eng. J.* **2019**, *366*, 264–304.
9. Chu, H.; Yang, W.; Sun, L.; Cai, S.; Yang, R.; Liang, W.; Yu, H.; Liu, L. 4D printing: A review on recent progresses. *Micromachines* **2020**, *11*, 796.

10. Le Duigou, A.; Chabaud, G.; Scarpa, F.; Castro, M. Bioinspired electro-thermo-hygro reversible shape-changing materials by 4D printing. *Adv. Funct. Mater.* **2019**, *29*, 1903280.
11. Jiang, Z.; Shen, P.; Tan, M.L.; Yan, Q.; Viktorova, J.; Cementon, C.; Peng, X.; Xiao, P.; Connal, L.A. 3D and 4D printable dual cross-linked polymers with high strength and humidity-triggered reversible actuation. *Mater. Adv.* **2021**, *2*, 5124–5134.
12. de Kergariou, C.; Demoly, F.; Perriman, A.; Le Duigou, A.; Scarpa, F. The Design of 4D-Printed Hygromorphs: State-of-the-Art and Future Challenges. *Adv. Funct. Mater.* **2023**, *33*, 2210353.
13. Al Nahari, B.; Zarbane, K.; Beidouri, Z. The use of moisture-responsive materials in 4D printing. *J. Achiev. Mater. Manuf. Eng.* **2023**, *119*, 5–13.
14. Dong, Y.; Wang, S.; Ke, Y.; Ding, L.; Zeng, X.; Magdassi, S.; Long, Y. 4D printed hydrogels: Fabrication, materials, and applications. *Adv. Mater. Technol.* **2020**, *5*, 2000034.
15. Tang, T.; Alfarhan, S.; Jin, K.; Li, X. 4D Printing of Seed Capsule-Inspired Hygro-Responsive Structures via Liquid Crystal Templating-Assisted Vat Photopolymerization. *Adv. Funct. Mater.* **2023**, *33*, 2211602.
16. Shanthamma, S.; Preethi, R.; Moses, J.; Anandharamakrishnan, C. 4D printing of sago starch with turmeric blends: A study on pH-triggered spontaneous color transformation. *ACS Food Sci. Technol.* **2021**, *1*, 669–679.
17. Teng, X.; Zhang, M.; Adhikari, B.; Ma, Y. 4D printed pH-responsive labels of methacrylic anhydride grafted konjac glucomannan for detecting quality changes in respiring climacteric fruits. *Food Hydrocoll.* **2024**, *149*, 109543.
18. Zhou, K.; Sun, R.; Wojciechowski, J.P.; Wang, R.; Yeow, J.; Zuo, Y.; Song, X.; Wang, C.; Shao, Y.; Stevens, M.M. 4D Multi-Material Printing of Soft Actuators with Spatial and Temporal Control. *Adv. Mater.* **2024**, 2312135.
19. Pan, H.M.; Goto, A. Topology-Dependent pH-Responsive Actuation and Shape Memory Programming for Biomimetic 4D Printing. *Macromol. Rapid Commun.* **2023**, *44*, 2300074.
20. Narupai, B.; Smith, P.T.; Nelson, A. 4D printing of multi-stimuli responsive protein-based hydrogels for autonomous shape transformations. *Adv. Funct. Mater.* **2021**, *31*, 2011012.
21. Chen, A.Y.; Pegg, E.; Chen, A.; Jin, Z.; Gu, G.X. 4D printing of electroactive materials. *Adv. Intell. Syst.* **2021**, *3*, 2100019.
22. Huang, X.; Panahi-Sarmad, M.; Dong, K.; Li, R.; Chen, T.; Xiao, X. Tracing evolutions in electro-activated shape memory polymer composites with 4D printing strategies: A systematic review. *Compos. Part A Appl. Sci. Manuf.* **2021**, *147*, 106444.
23. Shao, L.-H.; Zhao, B.; Zhang, Q.; Xing, Y.; Zhang, K. 4D printing composite with electrically controlled local deformation. *Extrem. Mech. Lett.* **2020**, *39*, 100793.
24. Lalegani Dezaki, M.; Bodaghi, M. Sustainable 4D printing of magneto-electroactive shape memory polymer composites. *Int. J. Adv. Manuf. Technol.* **2023**, *126*, 35–48.
25. Fu, P.; Li, H.; Gong, J.; Fan, Z.; Smith, A.T.; Shen, K.; Khalfalla, T.O.; Huang, H.; Qian, X.; McCutcheon, J.R. 4D printing of polymers: Techniques, materials, and prospects. *Prog. Polym. Sci.* **2022**, *126*, 101506.
26. Zhang, Y.; Wang, Q.; Yi, S.; Lin, Z.; Wang, C.; Chen, Z.; Jiang, L. 4D printing of magnetoactive soft materials for on-demand magnetic actuation transformation. *ACS Appl. Mater. Interfaces* **2021**, *13*, 4174–4184.
27. Liu, H.; Wang, F.; Wu, W.; Dong, X.; Sang, L. 4D printing of mechanically robust PLA/TPU/Fe₃O₄ magneto-responsive shape memory polymers for smart structures. *Compos. Part B Eng.* **2023**, *248*, 110382.
28. Simińska-Stanny, J.; Nizioł, M.; Szymczyk-Ziółkowska, P.; Brożyna, M.; Junka, A.; Shavandi, A.; Podstawczyk, D. 4D printing of patterned multimaterial magnetic hydrogel actuators. *Addit. Manuf.* **2022**, *49*, 102506.
29. Zhao, W.; Zhang, F.; Leng, J.; Liu, Y. Personalized 4D printing of bioinspired tracheal scaffold concept based on magnetic stimulated shape memory composites. *Compos. Sci. Technol.* **2019**, *184*, 107866.
30. Zhang, F.; Wang, L.; Zheng, Z.; Liu, Y.; Leng, J. *Magnetic Programming of 4D Printed Shape Memory Composite Structures*; Elsevier: Amsterdam, The Netherlands, 2019.
31. McLellan, K.; Li, T.; Sun, Y.-C.; Jakubinek, M.B.; Naguib, H.E. 4D printing of MXene composites for deployable actuating structures. *ACS Appl. Polym. Mater.* **2022**, *4*, 8774–8785.
32. Niazy, D.; Ashraf, M.; Bodaghi, M.; Zolfagharian, A. Resilient city perspective: 4D printing in art, architecture and construction. *Mater. Today Sustain.* **2024**, 100708.
33. Lyu, Z.; Wang, J.; Chen, Y. 4D printing: Interdisciplinary integration of smart materials, structural design, and new functionality. *Int. J. Extrem. Manuf.* **2023**, *5*, 032011.
34. Nas, M.O. 4D Printing of Hygroscopic Wood Based Actuators for Climate Responsive Skin. Master's Thesis, Middle East Technical University, Ankara, Turkey, 2023.
35. Li, S. Review on development and application of 4D-printing technology in smart textiles. *J. Eng. Fibers Fabr.* **2023**, *18*, 15589250231177448.
36. Biswas, M.C.; Chakraborty, S.; Bhattacharjee, A.; Mohammed, Z. 4D printing of shape memory materials for textiles: Mechanism, mathematical modeling, and challenges. *Adv. Funct. Mater.* **2021**, *31*, 2100257.
37. Manaia, J.P.; Cerejo, F.; Duarte, J. Revolutionising textile manufacturing: A comprehensive review on 3D and 4D printing technologies. *Fash. Text.* **2023**, *10*, 20.
38. Zhang, Z.; Demir, K.G.; Gu, G.X. Developments in 4D-printing: A review on current smart materials, technologies, and applications. *Int. J. Smart Nano Mater.* **2019**, *10*, 205–224.
39. Zeng, S.; Gao, Y.; Tan, J.; Wei, Z. Self-Assembly by 4D Printing: Design and Fabrication of Sequential Self-Folding. In *Smart Materials, Adaptive Structures and Intelligent Systems*; American Society of Mechanical Engineers: New York, NY, USA, 2022; Volume 86274, p. V001T03A005.

40. An, B.; Tao, Y.; Gu, J.; Cheng, T.; Chen, X.A.; Zhang, X.; Zhao, W.; Do, Y.; Takahashi, S.; Wu, H.-Y. Thermorph: Democratizing 4D printing of self-folding materials and interfaces. In Proceedings of the 2018 CHI Conference on Human Factors in Computing Systems, Montreal, QC, Canada, 21–26 April 2018; pp. 1–12.
41. Deng, D.; Chen, Y. 4D printing: Design and fabrication of 3D shell structures with curved surfaces using controlled self-folding. In Proceedings of the International Manufacturing Science and Engineering Conference, London, UK, 1–3 July 2015; American Society of Mechanical Engineers: New York, NY, USA, 2015; Volume 56826, p. V001T02A070.
42. Zhao, W.; Li, N.; Liu, L.; Leng, J.; Liu, Y. Origami derived self-assembly stents fabricated via 4D printing. *Compos. Struct.* **2022**, *293*, 115669.
43. Li, X.; Shang, J.; Wang, Z. Intelligent materials: A review of applications in 4D printing. *Assem. Autom.* **2017**, *37*, 170–185.
44. Subeshan, B.; Baddam, Y.; Asmatulu, E. Current progress of 4D-printing technology. *Prog. Addit. Manuf.* **2021**, *6*, 495–516.
45. McLellan, K.; Sun, Y.-C.; Naguib, H.E. A review of 4D printing: Materials, structures, and designs towards the printing of biomedical wearable devices. *Bioprinting* **2022**, *27*, e00217.
46. Wang, Y.; Cui, H.; Esworthy, T.; Mei, D.; Wang, Y.; Zhang, L.G. Emerging 4D printing strategies for next-generation tissue regeneration and medical devices. *Adv. Mater.* **2022**, *34*, 2109198.
47. Ramezani, M.; Mohd Ripin, Z. 4D printing in biomedical engineering: Advancements, challenges, and future directions. *J. Funct. Biomater.* **2023**, *14*, 347.
48. Khalid, M.Y.; Arif, Z.U.; Noroozi, R.; Zolfagharian, A.; Bodaghi, M. 4D printing of shape memory polymer composites: A review on fabrication techniques, applications, and future perspectives. *J. Manuf. Process.* **2022**, *81*, 759–797.
49. Hann, S.Y.; Cui, H.; Nowicki, M.; Zhang, L.G. 4D printing soft robotics for biomedical applications. *Addit. Manuf.* **2020**, *36*, 101567.
50. Khalid, M.Y.; Arif, Z.U.; Ahmed, W.; Umer, R.; Zolfagharian, A.; Bodaghi, M. 4D printing: Technological developments in robotics applications. *Sens. Actuators A Phys.* **2022**, *343*, 113670.
51. Soleimanzadeh, H.; Rolfe, B.; Bodaghi, M.; Jamalabadi, M.; Zhang, X.; Zolfagharian, A. Sustainable robots 4D printing. *Adv. Sustain. Syst.* **2023**, *7*, 2300289.
52. Mei, S.; Wang, J.; Li, Z.; Ding, B.; Li, S.; Chen, X.; Zhao, W.; Zhang, Y.; Zhang, X.; Cui, Z. 4D printing of polyamide 1212 based shape memory thermoplastic polyamide elastomers by selective laser sintering. *J. Manuf. Process.* **2023**, *92*, 157–164.
53. Weber, R.; Kuhlow, M.; Spierings, A.B.; Wegener, K. 4D printed assembly of sensors and actuators in complex formed metallic lightweight structures. *J. Manuf. Process.* **2023**, *90*, 406–417.
54. Zhan, J.; Wu, J.; Ma, R.; Li, K.; Lin, J.; Murr, L.E. Tuning the functional properties by laser powder bed fusion with partitioned repetitive laser scanning: Toward edTable 4D printing of NiTi alloys. *J. Manuf. Process.* **2023**, *101*, 1468–1481.
55. Singh, S.; Singh, G.; Prakash, C.; Ramakrishna, S. Current status and future directions of fused filament fabrication. *J. Manuf. Process.* **2020**, *55*, 288–306.
56. Dey, A.; Yodo, N. A systematic survey of FDM process parameter optimization and their influence on part characteristics. *J. Manuf. Mater. Process.* **2019**, *3*, 64.
57. Xiao, R.; Nguyen, T.D. Thermo-mechanics of amorphous shape-memory polymers. *Procedia Iutam* **2015**, *12*, 154–161.
58. Carrell, J.; Gruss, G.; Gomez, E. Four-dimensional printing using fused-deposition modeling: A review. *Rapid Prototyp. J.* **2020**, *26*, 855–869.
59. Khalid, M.Y.; Arif, Z.U.; Ahmed, W. 4D printing: Technological and manufacturing renaissance. *Macromol. Mater. Eng.* **2022**, *307*, 2200003.
60. Soleyman, E.; Aberoumand, M.; Soltanmohammadi, K.; Rahmatabadi, D.; Ghasemi, I.; Baniassadi, M.; Abrinia, K.; Baghani, M. 4D printing of PET-G via FDM including tailormade excess third shape. *Manuf. Lett.* **2022**, *33*, 1–4.
61. Barletta, M.; Gisario, A.; Mehrpouya, M. 4D printing of shape memory polylactic acid (PLA) components: Investigating the role of the operational parameters in fused deposition modelling (FDM). *J. Manuf. Process.* **2021**, *61*, 473–480.
62. Aberoumand, M.; Rahmatabadi, D.; Soltanmohammadi, K.; Soleyman, E.; Ghasemi, I.; Baniassadi, M.; Abrinia, K.; Bodaghi, M.; Baghani, M. Stress Recovery and Stress Relaxation Behaviors of PVC 4D Printed by FDM Technology for High-Performance Actuation Applications. *Sens. Actuators A Phys.* **2023**, 114572.
63. Yu, Y.; Liu, H.; Qian, K.; Yang, H.; McGehee, M.; Gu, J.; Luo, D.; Yao, L.; Zhang, Y.J. Material characterization and precise finite element analysis of fiber reinforced thermoplastic composites for 4D printing. *Comput.-Aided Des.* **2020**, *122*, 102817.
64. Nguyen, T.T.; Kim, J. 4D-printing—Fused deposition modeling printing and PolyJet printing with shape memory polymers composite. *Fibers Polym.* **2020**, *21*, 2364–2372.
65. Bodaghi, M.; Serjouei, A.; Zolfagharian, A.; Fotouhi, M.; Rahman, H.; Durand, D. Reversible energy absorbing meta-sandwiches by FDM 4D printing. *Int. J. Mech. Sci.* **2020**, *173*, 105451.
66. Wang, Y.; Li, X. 4D-printed bi-material composite laminate for manufacturing reversible shape-change structures. *Compos. Part B Eng.* **2021**, *219*, 108918.
67. Nezhad, I.S.; Golzar, M.; Behraves, A.H.; Zare, S. Comprehensive study on shape shifting behaviors in FDM-based 4D printing of bilayer structures. *Int. J. Adv. Manuf. Technol.* **2022**, *120*, 959–974.
68. Moradi, M.; Dezaki, M.L.; Kheyri, E.; Rasouli, S.A.; Attar, M.A.; Bodaghi, M. Simultaneous FDM 4D printing and magnetizing of iron-filled polylactic acid polymers. *J. Magn. Magn. Mater.* **2023**, *568*, 170425.
69. Zhang, Q.; Yan, D.; Zhang, K.; Hu, G. Pattern transformation of heat-shrinkable polymer by three-dimensional (3D) printing technique. *Sci. Rep.* **2015**, *5*, 8936.

70. Wang, G.; Yang, H.; Yan, Z.; Gecer Ulu, N.; Tao, Y.; Gu, J.; Kara, L.B.; Yao, L. 4DMesh: 4D printing morphing non-developable mesh surfaces. In Proceedings of the 31st Annual ACM Symposium on User Interface Software and Technology, Berlin, Germany, 14–17 October 2018; pp. 623–635.
71. Gu, J.; Breen, D.E.; Hu, J.; Zhu, L.; Tao, Y.; Van de Zande, T.; Wang, G.; Zhang, Y.J.; Yao, L. Geodesy: Self-rising 2.5 d tiles by printing along 2d geodesic closed path. In Proceedings of the 2019 CHI Conference on Human Factors in Computing Systems, Scotland, UK, 4–9 May 2019; pp. 1–10.
72. Wang, G.; Tao, Y.; Capunaman, O.B.; Yang, H.; Yao, L. A-line: 4D printing morphing linear composite structures. In Proceedings of the 2019 CHI Conference on Human Factors in Computing Systems, Scotland, UK, 4–9 May 2019; pp. 1–12.
73. Wu, P.; Yu, T.; Chen, M.; Hui, D. Effect of printing speed and part geometry on the self-deformation behaviors of 4D printed shape memory PLA using FDM. *J. Manuf. Process.* **2022**, *84*, 1507–1518.
74. Hosseinzadeh, M.; Ghoreishi, M.; Narooei, K. 4D printing of shape memory polylactic acid beams: An experimental investigation into FDM additive manufacturing process parameters, mathematical modeling, and optimization. *J. Manuf. Process.* **2023**, *85*, 774–782.
75. Wang, Y.; Li, X. An accurate finite element approach for programming 4D-printed self-morphing structures produced by fused deposition modeling. *Mech. Mater.* **2020**, *151*, 103628.
76. Goo, B.; Hong, C.-H.; Park, K. 4D printing using anisotropic thermal deformation of 3D-printed thermoplastic parts. *Mater. Des.* **2020**, *188*, 108485.
77. Samy, A.A.; Golbang, A.; Harkin-Jones, E.; Archer, E.; Tormey, D.; McIlhagger, A. Finite element analysis of residual stress and warpage in a 3D printed semi-crystalline polymer: Effect of ambient temperature and nozzle speed. *J. Manuf. Process.* **2021**, *70*, 389–399.
78. Santos, T.; Belbut, M.; Amaral, J.; Amaral, V.; Ferreira, N.; Alves, N.; Pascoal-Faria, P. Insights into Temperature Simulation and Validation of Fused Deposition Modeling Processes. *J. Manuf. Mater. Process.* **2023**, *7*, 189.
79. Dubey, D.; Mirhakimi, A.S.; Elbestawi, M.A. Negative Thermal Expansion Metamaterials: A Review of Design, Fabrication, and Applications. *J. Manuf. Mater. Process.* **2024**, *8*, 40.
80. Li, S.; Wang, K. Plant-inspired adaptive structures and materials for morphing and actuation: A review. *Bioinspiration Biomim.* **2016**, *12*, 011001.
81. Lachenal, X.; Daynes, S.; Weaver, P.M. Review of morphing concepts and materials for wind turbine blade applications. *Wind Energy* **2013**, *16*, 283–307.
82. Chillara, V.; Dapino, M. Review of morphing laminated composites. *Appl. Mech. Rev.* **2020**, *72*, 010801.
83. Koirala, S.; Prakash, S.; Karim, A.; Bhandari, B. Shape morphing of foods: Mechanism, strategies, and applications. *Trends Food Sci. Technol.* **2023**, 104135.
84. Ren, L.; Wang, Z.; Ren, L.; Xu, C.; Li, B.; Shi, Y.; Liu, Q. Understanding the role of process parameters in 4D printing: A review. *Compos. Part B Eng.* **2023**, 110938.
85. Kumar, R.; Singh, R.; Farina, I. On the 3D printing of recycled ABS, PLA and HIPS thermoplastics for structural applications. *PSU Res. Rev.* **2018**, *2*, 115–137.
86. Lee, J.-Y.; An, J.; Chua, C.K. Fundamentals and applications of 3D printing for novel materials. *Appl. Mater. Today* **2017**, *7*, 120–133.
87. Rodríguez-Panes, A.; Claver, J.; Camacho, A.M. The influence of manufacturing parameters on the mechanical behaviour of PLA and ABS pieces manufactured by FDM: A comparative analysis. *Materials* **2018**, *11*, 1333.
88. Rutkowski, J.V.; Levin, B.C. Acrylonitrile–butadiene–styrene copolymers (ABS): Pyrolysis and combustion products and their toxicity—A review of the literature. *Fire Mater.* **1986**, *10*, 93–105.
89. Kumar, S.; Kruth, J.-P. Composites by rapid prototyping technology. *Mater. Des.* **2010**, *31*, 850–856.
90. Pringle, A.M.; Rudnicki, M.; Pearce, J.M. Wood furniture waste-based recycled 3-D printing filament. *For. Prod. J.* **2018**, *68*, 86–95.
91. Cattenone, A.; Morganti, S.; Alaimo, G.; Auricchio, F. Finite element analysis of additive manufacturing based on fused deposition modeling: Distortions prediction and comparison with experimental data. *J. Manuf. Sci. Eng.* **2019**, 141.
92. Li, L.; Sun, Q.; Bellehumeur, C.; Gu, P. Investigation of bond formation in FDM process. In Proceedings of the 2002 International Solid Freeform Fabrication Symposium, Austin, TX, USA, 5–7 August 2002.
93. Morgan, R.V.; Reid, R.S.; Baker, A.M.; Lucero, B.; Bernardin, J.D. *Emissivity Measurements of Additively Manufactured Materials*; Los Alamos National Lab.(LANL): Los Alamos, NM, USA, 2017.
94. Armillotta, A.; Bellotti, M.; Cavallaro, M. Warpage of FDM parts: Experimental tests and analytic model. *Robot. Comput.-Integr. Manuf.* **2018**, *50*, 140–152.
95. Hieber, C.A. Melt-viscosity characterization and its application to injection molding. In *Injection and Compression Molding Fundamentals*; Routledge: London, UK, 2017; pp. 1–136.
96. Richeton, J.; Ahzi, S.; Vecchio, K.S.; Jiang, F.C.; Adharapurapu, R.R. Influence of temperature and strain rate on the mechanical behavior of three amorphous polymers: Characterization and modeling of the compressive yield stress. *Int. J. Solids Struct.* **2006**, *43*, 2318–2335.
97. Song, P.; Cao, Z.; Meng, Q.; Fu, S.; Fang, Z.; Wu, Q.; Ye, J. Effect of lignin incorporation and reactive compatibilization on the morphological, rheological, and mechanical properties of ABS resin. *J. Macromol. Sci. Part B* **2012**, *51*, 720–735.

98. British Standard/International Organization for Standardization. Borosilicate Glass 3.3—Properties (BS ISO Standard No. 3585:1998), 1998. Available online: <https://www.iso.org/standard/24774.html> (accessed on 10 April 2024).
99. Huang, Y.; Löschke, S.; Proust, G. In the mix: The effect of wood composition on the 3D printability and mechanical performance of wood-plastic composites. *Compos. Part C Open Access* **2021**, *5*, 100140.
100. Bi, X.; Huang, R. 3D printing of natural fiber and composites: A state-of-the-art review. *Mater. Des.* **2022**, *222*, 111065.
101. Mussa, H.M.; Salih, T.W.M. Experimental Investigation on Thermal Properties of Wood-Plastic Composites as Flat Panels. *J. Eng. Res.* **2021**, *9*. <http://doi.org/10.36909/jer.v9i1CRIE.11675>.

Disclaimer/Publisher's Note: The statements, opinions and data contained in all publications are solely those of the individual author(s) and contributor(s) and not of MDPI and/or the editor(s). MDPI and/or the editor(s) disclaim responsibility for any injury to people or property resulting from any ideas, methods, instructions or products referred to in the content.